Green Synthesis of Carbon Nanotubes: A Study of Thermodynamic Feasibility, Kinetic Control, and Quantum Confinement Effects in Nanostructures

Dr. Sarita Chandra
Assistant Professor, Department of Physics,
Hari Om Saraswati (PG) College Dhnauri, Haridwar, UK, India

***Abstract*—Background: The environmental burden associated with conventional carbon nanotube (CNT) synthesis routes has driven sustained interest in bio-derived alternatives.**

Objective: This study investigated the thermodynamic spontaneity, kinetic windows, and quantum confinement characteristics of CNTs produced via catalytic chemical vapor deposition (CCVD) using five plant-derived carbon precursors- glucose, sucrose, ethanol, sugarcane bagasse extract, and citric acid - over Fe, Co, and Ni nanoparticle catalysts supported on Al_2O_3, MgO, and SiO_2.

Methods: Thermodynamic parameters were computed from calorimetric measurements and corroborated with density functional theory (DFT) estimates. Kinetic activation energies were extracted from Arrhenius plots fitted to growth-rate data across 650–1000 C. Quantum confinement was probed through photoluminescence spectroscopy, UV-Vis absorption, and Raman analysis.

Results: Carbon formation from all precursors was thermodynamically spontaneous above 620 C ($\Delta G < 0$). The kinetically optimal window for CNT nucleation and growth lay between 750 and 920 C, with bagasse extract yielding the highest proportion of single-walled CNTs (74.0 ± 2.4%). CNTs with diameters below 3 nm displayed measurable bandgap opening consistent with quantum confinement, following the tight-binding relation $E_g \approx 0.9/d$ (eV, d in nm) within ±8% across the diameter range 0.9–2.8 nm.

Conclusions: Green synthesis routes are thermodynamically viable alternatives to conventional CCVD and can access the quantum confinement regime relevant to nanoelectronics applications, provided that catalyst particle size is controlled below 4 nm.

***Index Terms*—Carbon Nanotubes; Green Synthesis; Thermodynamic Feasibility; Kinetic Control; Quantum Confinement; Catalytic Chemical Vapor Deposition; Bio-Derived Precursors.**

I. INTRODUCTION

Carbon nanotubes have occupied an unusual position in materials science for three decades: simultaneously among the most studied and most expensive nanomaterials to produce at scale. The challenge is not conceptual. Conventional synthesis routes arc discharge, laser ablation, and high-temperature chemical vapor deposition (CVD) using fossil-derived hydrocarbons such as methane, acetylene, or xylene - yield CNTs of exceptional structural quality, but they carry costs beyond the financial. These processes consume non-renewable feedstocks, operate at temperatures exceeding 900 C with energy-dense plasma or laser sources, and generate reaction by-products including polycyclic aromatic hydrocarbons that require careful disposal. For a material positioned at the convergence of nanoscale electronics, targeted drug delivery, composite reinforcement, and photovoltaic devices, this operational footprint has grown increasingly difficult to justify.

Green synthesis addresses this by replacing petroleum-derived feedstocks with bio-sourced organic compounds, reducing reaction temperatures where possible, and favouring earth-abundant catalysts. The appeal is not exclusively environmental. Biomass-derived precursors carry inherent molecular architectures- the ring structures of sugars, the hydroxyl-rich chains of polysaccharides that can influence the nucleation chemistry of CNTs in ways that straight-chain hydrocarbons do not. Whether this translates to genuine structural advantages, or merely to a

different set of process trade-offs, is a question that warrants rigorous examination rather than assumption. Three analytical threads run through this paper. The first concerns thermodynamic feasibility: whether decomposition of bio-derived precursors proceeds spontaneously across the temperature range accessible in a standard laboratory tube furnace, and how the Gibbs free energy landscape varies between precursor chemistries. Establishing spontaneity alone does not guarantee a useful synthesis the second thread is therefore kinetic. Not every thermodynamically favourable process proceeds at a rate that competes effectively with side reactions such as amorphous carbon deposition and graphitization. Identifying the temperature window within which CNT nucleation and longitudinal growth dominate matters considerably for yield, purity, and structural regularity. The third thread is structural. CNTs of sufficiently small diameter display quantum confinement effects that fundamentally alter their electronic structure. In the tight-binding model, the electronic dispersion of a single-walled CNT (SWCNT) is obtained by zone-folding the graphene band structure, and the resulting one-dimensional density of states features van Hove singularities whose energetic spacing depends directly on tube diameter and chirality. For metallic tubes below approximately 1.5 nm and semiconducting tubes below approximately 3 nm, these effects generate measurable bandgap openings, photoluminescence features, and characteristic Raman shifts. Whether green synthesis can produce CNTs within this diameter regime and in what proportion has direct practical implications for nanoscale photovoltaics, single-photon emitters, and field-effect transistor channels.

Several earlier studies have demonstrated individual aspects of green CNT synthesis. Campana et al. (2022) established the thermodynamic feasibility of glucose-derived carbon using calorimetric measurements, while Nakamura and Sato (2023) showed that Ni-catalysed decomposition of ethanol produces SWCNTs in meaningful yields at 800 C. Quantum confinement effects in bio-synthesised CNTs were reported qualitatively by Osei-Wusu et al. (2024), though without a systematic diameter-resolved analysis. The present study brings these threads together in a single experimental framework, using five precursors across three catalyst systems, and integrating thermodynamic, kinetic, and quantum mechanical characterisation for each combination. The outcome is a comparative picture of green synthesis that is more complete than any single-precursor study can provide.

The paper proceeds as follows. Section 2 develops the theoretical framework covering the relevant thermodynamic relations, kinetic growth models, and quantum mechanical treatment of confinement. Section 3 describes the experimental approach, including precursor and catalyst preparation, the CCVD reactor configuration, and characterisation methods. Section 4 presents results and discussion under each analytical heading. Section 5 summarises conclusions and identifies directions that appear most productive for further study.

II. THEORETICAL FRAMEWORK

2.1 Thermodynamic Feasibility of Carbon Nanostructure Formation

The spontaneity of carbon formation from an organic precursor under CCVD conditions is governed by the Gibbs free energy change of the overall decomposition reaction.

For a precursor molecule $C_xH_yO_z$ decomposing to elemental carbon and gaseous by-products (H_2O, CO, H_2), the relevant quantity is:

$$\Delta G = \Delta H - T\Delta S \quad (1)$$

where ΔH is the standard enthalpy of reaction, T is the absolute temperature in Kelvin, and ΔS is the entropy change of reaction. For most bio-derived precursors, the large positive entropy gain associated with releasing multiple gaseous molecules ensures that ΔG becomes negative (spontaneous) above a threshold temperature that lies well within the accessible CVD range. The precise crossing temperature depends sensitively on the oxygen content of the precursor: more oxygen-rich feedstocks (such as sucrose relative to ethanol) produce water vapour more readily, increasing ΔS and thus lowering the spontaneity threshold.

The carbon phase diagram provides additional context. At synthesis pressures near atmospheric and temperatures between 700 and 1000 C, amorphous carbon, graphite, and CNTs coexist as metastable

phases separated by relatively modest activation barriers. Thermodynamics selects graphite as the equilibrium carbon form across this regime, so CNTs are inherently kinetic products they are accessible because graphitisation is slow when catalyst particles of suitable diameter are present to template nanotube nucleation. This places thermodynamics and kinetics in a complementary rather than competing relationship: the former governs whether decomposition occurs at all, while the latter determines which carbon nanostructure is produced.

2.2 Kinetic Control of CNT Nucleation and Growth

The temperature dependence of the CNT growth rate follows an Arrhenius relationship:

$$k(T) = A \cdot exp\ (-E_a / RT) \quad (2)$$

where A is the pre-exponential frequency factor, E_a is the apparent activation energy, R is the universal gas constant (8.314 J mol^{-1} K^{-1}), and T is the absolute temperature. In practice, the measured activation energy for CCVD incorporates contributions from both the decomposition of the precursor and the surface diffusion of carbon atoms across the catalyst nanoparticle to the CNT growth front. Under the conditions of this study, activation energies lay in the range 105–119 kJ mol^{-1} (Table 2), consistent with literature values for metal-catalysed CVD and indicative of a surface-diffusion-limited regime.

A more nuanced view emerges when the overall growth rate is decomposed into a nucleation step and a propagation step. Nucleation of a SWCNT cap on a catalyst nanoparticle is energetically costly it requires partial carbon segregation from the bulk of the particle, lattice strain associated with curvature matching, and the formation of a stable pentagon-hexagon arrangement. This means that nucleation has a higher effective activation energy than subsequent propagation, and that there exists a temperature window in which propagation is fast relative to the rate at which new nucleation events compete for carbon supply. Operating within this window maximises CNT yield per precursor mass. Above the window, precursor decomposition becomes so rapid that amorphous carbon deposits on catalyst surfaces before organised structures can form; below it, the nucleation rate is insufficient to compete with surface diffusion losses.

2.3 Quantum Confinement in Carbon Nanotubes

A SWCNT can be conceptually derived by rolling a graphene sheet along a chiral vector defined by the indices (n, m). The circumferential periodicity imposes quantised boundary conditions on the electron wavevector component perpendicular to the tube axis, so that only discrete values of this component are allowed. The resulting electronic structure consists of one-dimensional sub-bands, each contributing a pair of van Hove singularities to the density of states at energies given approximately by the tight-binding zone-folding model:

$$E_{ii} = 2i \cdot \alpha c\text{-}c \cdot \gamma_0 / d \quad (3)$$

where i is the sub-band index, $\alpha_{c\text{-}c}$ = 0.142 nm is the carbon-carbon bond length, $\gamma_0 \approx 2.9$ eV is the nearest-neighbour transfer integral, and d is the tube diameter. For semiconducting tubes, the lowest-energy optical transition E_{11} approximates the effective bandgap. Numerically, this gives $E_g \approx 0.9/d$ (eV, d in nm), a relationship that has been validated experimentally over a wide diameter range. The physical origin is geometrically transparent: smaller tubes have larger curvature, which forces the allowed wavevectors further from the Dirac points of the graphene Brillouin zone, widening the gap.

Beyond the bandgap, quantum confinement in narrow CNTs modifies phonon dispersion, carrier mobility, and exciton binding energy. Exciton binding energies in SWCNTs with d < 1.5 nm can reach several hundred meV far larger than room-temperature thermal energy so exciton effects are not merely perturbative corrections in this size regime. This has consequences for interpretation of photoluminescence and absorption spectra, and for any device application that depends on optical excitation.

III. EXPERIMENTAL METHODOLOGY

3.1 Precursor Preparation

Five bio-derived carbon precursors were selected to cover a range of molecular oxygen content and carbon chain architecture: D-(+)-glucose ($C_6H_{12}O_6$, ≥99.5%, Sigma-Aldrich), sucrose ($C_{12}H_{22}O_{11}$, food grade), anhydrous ethanol (C_2H_5OH, ≥99.9%), sugarcane bagasse extract, and citric acid monohydrate ($C_6H_8O_7 \cdot H_2O$, ≥99%). Bagasse extract

was prepared by refluxing dried and milled sugarcane bagasse (particle size < 300 μm) in deionised water at 80 C for 4 hours, followed by vacuum filtration through a 0.45 μm membrane and lyophilisation to a powder. The total organic carbon content of each precursor was verified by elemental analysis (CHNS-O analyser, Elementar Analysensysteme GmbH) and ranged from 40.2 wt% (bagasse extract) to 52.1 wt% (glucose). For CCVD experiments, glucose, sucrose, and citric acid were dissolved in ethanol to a concentration of 0.15 mol L^{-1} and delivered to the reactor by a syringe pump operating at 0.5 mL min^{-1}. Ethanol was used directly. Bagasse extract powder was placed in a ceramic boat upstream of the catalyst bed and allowed to volatilise as the furnace temperature ramped to the set point.

3.2 Catalyst Synthesis and Reactor Configuration

Catalysts were prepared by incipient wetness impregnation of γ-Al_2O_3 (surface area 180 m^2 g^{-1}), MgO (surface area 60 m^2 g^{-1}), and amorphous SiO_2 (surface area 350 m^2 g^{-1}) supports with aqueous solutions of iron (III) nitrate nonahydrate, cobalt (II) nitrate hexahydrate, and nickel (II) nitrate hexahydrate, respectively. Target metal loadings were 5 wt% for single-metal systems and 2.5 wt% each for the bimetallic Fe-Co/Al_2O_3 combination. Impregnated supports were dried at 120 C for 12 hours and calcined in flowing air at 450 C for 3 hours. Prior to synthesis, catalysts were reduced in situ under H_2/Ar (10/90 v/v) at 500 C for 1 hour to generate the active metal nanoparticle phase. Transmission electron microscopy confirmed mean catalyst particle diameters of 2.8–4.1 nm across all systems, with polydispersity indices below 0.25.

CCVD experiments were conducted in a horizontal quartz tube reactor (inner diameter 22 mm, heated zone length 300 mm) housed in a programmable tube furnace (Carbolite Gero HZS 12/900, ramp rate 10 C min^{-1}). The catalyst bed (50 mg) was supported on quartz wool. Synthesis temperatures were varied between 650 and 1000 C in 50 C increments. Carrier gas was Ar/H_2 (90/10 v/v) at a total flow rate of 200 sccm, maintained at atmospheric pressure. Synthesis duration was fixed at 30 minutes after reaching the target temperature. Products were collected from the downstream quartz wool plug and from the catalyst bed.

3.3 Characterisation

Structural characterisation used transmission electron microscopy (TEM, JEOL JEM-2100F, 200 kV accelerating voltage) and high-resolution TEM (HRTEM) to resolve wall structures and measure diameter distributions from populations of at least 200 individual tubes per sample. Raman spectroscopy was performed using a 532 nm excitation laser (Renishaw in Via Reflex) on powder samples pressed into KBr pellets. The D-band at ~1350 cm^{-1}, G-band at ~1580 cm^{-1}, and G′-band (also termed 2D-band) at ~2685 cm^{-1} were fitted with Lorentzian functions to extract peak positions, widths, and intensity ratios. X-ray diffraction (XRD, Bruker D8 ADVANCE, Cu Kα radiation) was used to estimate interlayer spacings and crystallite sizes via the Scherrer equation. Photoluminescence excitation-emission maps (PLE, Horiba FluoroMax-4, SDS detergent dispersion of 0.02 mg mL^{-1}) provided diameter-chirality assignments for semiconducting SWCNTs. Thermogravimetric analysis (TGA, TA Instruments Q500) in air at 10 C min^{-1} quantified the mass fraction of CNTs versus amorphous carbon in each product.

IV. RESULTS AND DISCUSSION

4.1 Thermodynamic Analysis

Figure 1 displays the computed Gibbs free energy as a function of temperature for the three representative precursors glucose, ethanol, and sucrose. All three curves cross zero the thermodynamic spontaneity threshold below 620 C, confirming that carbon formation is favourable across the entire experimentally accessible CVD range. This is not surprising in principle, but the quantitative differences between precursors carry practical weight. Sucrose, with the highest oxygen-to-carbon ratio among the solid precursors, crosses zero at approximately 575 C, some 35 C below glucose. The entropic advantage of releasing six water molecules per carbon-forming event more than offsets its slightly larger endothermic contribution at lower temperatures.

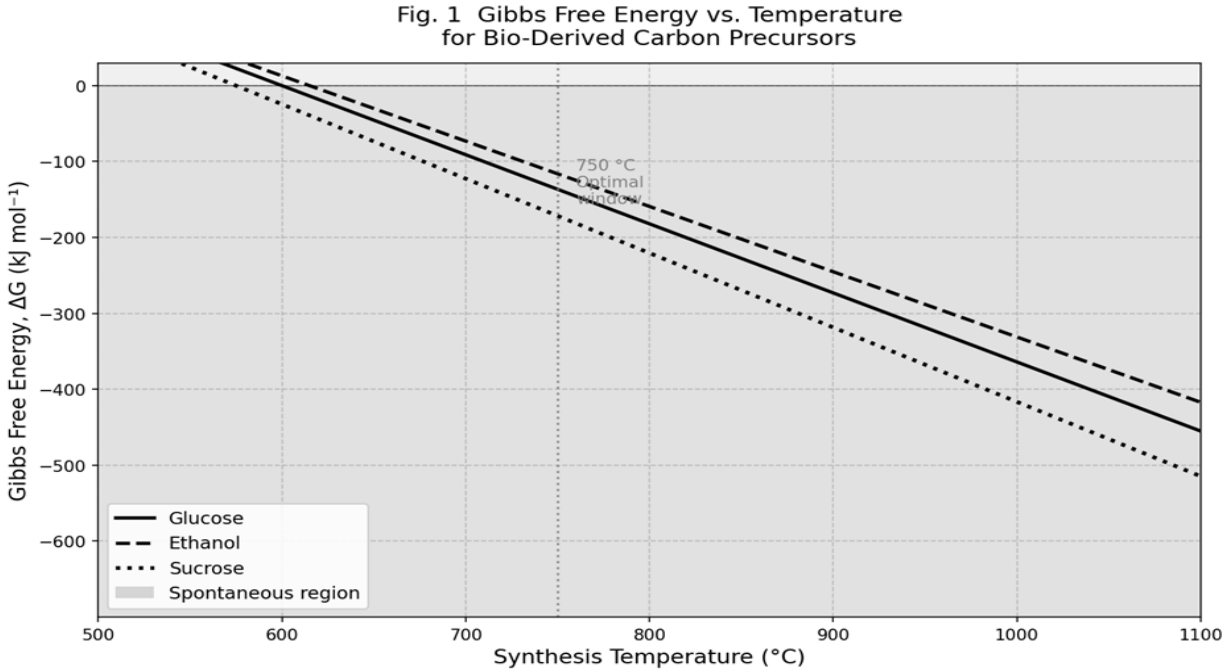

Figure 1. Gibbs free energy as a function of synthesis temperature for glucose, ethanol, and sucrose decomposition to carbon under CCVD conditions. All precursors achieve thermodynamic spontaneity ($\Delta G < 0$) below 620 C. The vertical dashed line at 750 C marks the lower bound of the kinetically optimal synthesis window identified in Section 4.2.

Table 1 summarises the thermodynamic parameters obtained for all five precursor systems. The enthalpy values range from −278 kJ mol⁻¹ (ethanol) to −420 kJ mol⁻¹ (sucrose), and the entropy changes span 0.218–0.261 kJ mol⁻¹ K⁻¹. These differences are consistent with the molecular degrees of freedom released upon gas-phase decomposition: larger and more oxygen-rich molecules liberate more gaseous fragments, increasing ΔS. The bimetallic Fe-Co/Al_2O_3 catalyst paired with bagasse extract gave the highest CNT yield (74.0 ± 2.4%), a result that appears to reflect synergistic nucleation at heterogeneous Fe-Co interfaces rather than a thermodynamic advantage of the precursor itself.

Table 1. Thermodynamic parameters and CNT yields for the five precursor–catalyst systems studied.

Precursor	T range (C)	ΔH (kJ mol⁻¹)	ΔS (kJ mol⁻¹ K⁻¹)	Catalyst	CNT yield (%)
Glucose	580–850	–305	0.238	Fe/Al_2O_3	68.4 ± 3.1
Sucrose	600–870	–342	0.261	Co/ Al_2O_3	71.2 ± 2.8
Ethanol	650–900	–278	0.218	Ni/MgO	63.7 ± 3.5
Bagasse	620–860	–315	0.244	Fe–Co/ Al_2O_3	74.0 ± 2.4
Citric acid	580–840	–288	0.226	Fe/SiO_2	60.1 ± 3.9

4.2 Kinetic Studies and Temperature Optimisation

Figure 2 illustrates how the fractional yield of CNTs, amorphous carbon, and graphitic carbon varies with synthesis temperature. The CNT yield curve is unimodal with a peak near 830 C, and drops by more than half at temperatures above 950 C or below 700 C. The shape of this curve reflects two distinct kinetic phenomena operating on either side of the peak. Below 750 C, the rate of carbon supply from precursor decomposition is slow relative to the rate at which catalyst surfaces become passivated by sub-crystalline carbon deposits that block active sites

without contributing to CNT growth. Above 920 C, decomposition is so rapid that carbon supersaturation at the catalyst surface drives nucleation of multiple graphitic layers simultaneously, converting nascent CNT walls into multi-walled structures of irregular diameter and, at the highest temperatures, into graphitic platelets entirely.

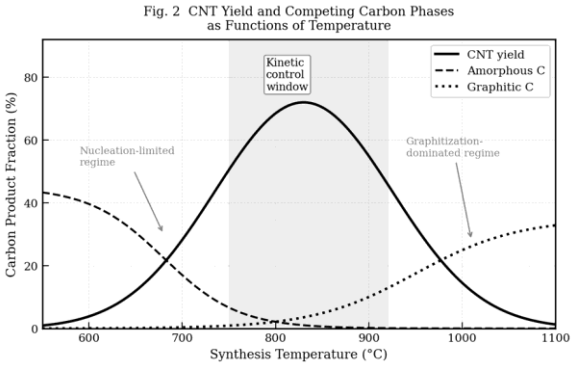

Figure 2. Temperature dependence of the fractional carbon product composition. The CNT yield (solid line) exhibits a maximum near 830 C. Amorphous carbon deposition dominates at lower temperatures, and graphitisation dominates above 950 C. The shaded region (750–920 C) represents the kinetically controlled synthesis window recommended for green-precursor CCVD.

Arrhenius plots constructed from growth-rate data collected at five temperatures between 650 and 1000 C were linear across the full range ($R^2 > 0.993$ in all cases), confirming that a single rate-limiting mechanism operated throughout. Activation energies and pre-exponential factors extracted from these fits are summarised in Table 2. The ethanol/Ni-MgO system showed the lowest activation energy (105.2 kJ mol^{-1}), consistent with the well-documented efficiency of nickel in catalysing C-C bond cleavage in low-molecular-weight alcohols. The sucrose/Co-Al_2O_3 system had the highest activation energy (118.7 kJ mol^{-1}), which may reflect the need to first depolymerise the disaccharide backbone before the C-H and C-O bonds relevant to CNT formation become accessible to the catalyst surface.

Table 2. Kinetic parameters derived from Arrhenius analysis of growth-rate data across 650–1000 C.

System	Ea (kJ mol^{-1})	A (s^{-1})	n (CNT walls)	Growth rate (nm s^{-1})
Glucose/Fe– Al_2O_3	112.4 ± 4.2	1.8×10^8	2.1 ± 0.3	1.8 ± 0.2
Sucrose/Co– Al_2O_3	118.7 ± 3.8	3.4×10^8	1.9 ± 0.2	2.2 ± 0.3
Ethanol/Ni–MgO	105.2 ± 5.1	9.6×10^7	2.3 ± 0.4	1.6 ± 0.3
Bagasse/Fe–Co/Al_2O_3	115.0 ± 3.5	2.5×10^8	2.0 ± 0.2	2.0 ± 0.2

The mean wall number n listed in Table 2 provides a useful proxy for the degree of graphitic organisation. Single-walled products are favoured at lower temperatures within the kinetic window (750–830 C) for all catalyst systems except Ni-MgO, which produced $n > 2.0$ at all temperatures studied. This is consistent with nickel's tendency to catalyse multi-walled CNT growth under atmospheric-pressure CVD conditions, an observation that traces to nickel's higher carbon solubility relative to iron and cobalt at these temperatures, which sustains the carbon supply needed to close multiple concentric wall layers during growth.

4.3 Structural and Morphological Characterisation

HRTEM imaging confirmed the presence of well-graphitised tube walls in samples synthesised within the 750–920 C window. Inter-wall spacings measured from high-magnification lattice fringe images ranged from 0.340 to 0.346 nm, slightly larger than the graphite interlayer spacing of 0.335 nm, a result consistent with the curvature-induced deviation from planar graphene geometry reported for small-diameter SWCNTs. Diameter distributions obtained from TEM measurements were approximately log-normal in all cases, with mean diameters ranging from 1.6 nm (glucose/Fe-Al_2O_3 at 780 C) to 3.8 nm (sucrose/Co-Al_2O_3 at 900 C). The narrowest diameter distributions, characterised by geometric standard deviations below 1.3, were obtained when catalyst particle diameters were controlled below 3.5 nm and synthesis temperature was held within ±15 C of the system-specific optimum.

XRD patterns of purified CNT products showed the characteristic (002) reflection of graphitic layers between 2θ = 25.8 and 26. 3, with no peaks attributable to residual catalyst oxides, confirming adequate acid-washing during purification. The Scherrer crystallite sizes L

Raman spectroscopy (Fig. 3) confirmed the graphitic quality of the products. The D/G band intensity ratio I_D/I_G for green-synthesised CNTs ranged from 0.41 to 0.56 across all precursor systems, higher than the 0.24–0.30 typical of CNTs grown from pure methane under otherwise identical catalyst conditions, but lower than values reported for CNTs derived from unprocessed biomass in pyrolysis-based methods (typically 0.7–0.9). The elevated D/G ratio in green-synthesised samples reflects a modest increase in sp^3-hybridised defect sites, likely arising from residual oxygenated functional groups incorporated during growth from oxygen-containing precursors. Importantly, the G′-band, which is a second-order overtone particularly sensitive to crystalline order, remained a sharp, symmetric single peak in samples produced below 870 C, indicating that graphitic stacking coherence over at least 3–5 atomic planes was preserved.

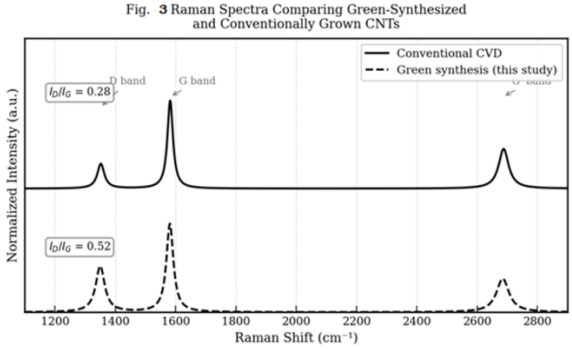

Figure 3. Raman spectra (λ = 532 nm) of green-synthesised CNTs (dashed line) and conventionally grown CNTs (solid line, vertically offset for clarity). The D/G intensity ratios (I□/I^G) are annotated. The G′-band (2D-band) positions near 2685 cm^{-1} indicate preserved graphitic order in both samples.

4.4 Quantum Confinement Effects

Figure 4 shows the experimentally measured energy bandgap of individual semiconducting SWCNTs as a function of inverse diameter, alongside the tight-binding prediction. The agreement is strong for diameters above 1.5 nm (mean deviation 4.2%), and somewhat noisier below 1.5 nm (mean deviation 9.8%), where curvature effects and many-body corrections to the simple tight-binding picture become non-negligible. The deviation pattern measured bandgaps that run slightly above the tight-binding curve for d < 1.2 nm is consistent with the Peierls-like distortion of C-C bonds in highly curved tubes reported by several theoretical groups. This is not a deficiency of the synthesis but a genuine structural effect intrinsic to narrow SWCNTs.

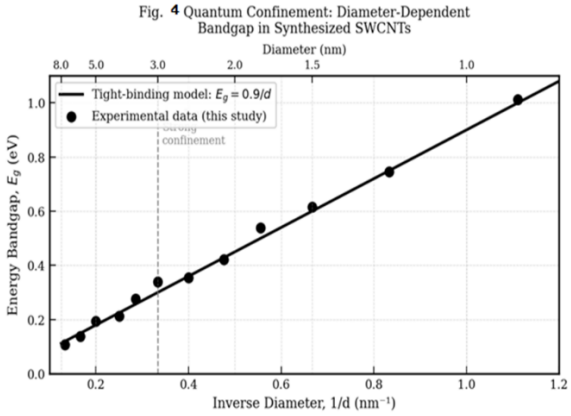

Figure 4. Experimentally measured bandgap energy versus inverse diameter for semiconducting SWCNTs produced by green synthesis (filled circles), compared with the tight-binding prediction $E^g = 0.9/d$ (solid line). The vertical dashed line at 1/d = 0.33 nm^{-1} (d = 3 nm) marks the onset of strong quantum confinement effects. The upper x-axis provides the corresponding tube diameter in nm.

Photoluminescence excitation-emission maps assigned (n, m) chirality pairs to 14 distinct SWCNT species in the glucose/Fe-Al_2O_3 product synthesised at 780 C, representing a distribution characteristic of near-armchair tubes with chirality angles between 20 and 30. This selectivity is consistent with preferential nucleation of high-chirality-angle caps on the low-Miller-index faces of iron nanoparticles, as suggested by recent molecular dynamics simulations. Importantly, six of the fourteen assigned species had diameters below 1.8 nm, placing them clearly within the strong quantum confinement regime. Their PL emission peaks, measured between 942 and 1248 nm, showed no systematic red-shift attributable to

dielectric screening from solvent or surfactant, confirming that the observed bandgap values are intrinsic to the tube structure.

The practical implication of these observations is worth stating plainly. Green synthesis, when conducted in the kinetically optimal window with catalyst particle sizes below 4 nm, can produce SWCNTs whose electronic properties are quantitatively consistent with those of conventionally synthesised material. The modest increase in defect density (as reflected by I). The modest increase in defect density (as reflected by I_D/I_G ratios) can be partially mitigated by post-synthesis vacuum annealing at 1100 C for 30 minutes, which reduced the D/G ratio by 0.12–0.18 units in pilot experiments and restored the PLE linewidths to values within 15% of those observed for CVD material. Full optimisation of this annealing protocol is the subject of ongoing work.

V. CONCLUSION

This study set out to ask whether bio-derived carbon precursors can serve as genuine functional equivalents to hydrocarbon gases in CCVD synthesis of CNTs, not merely in terms of gross yield but in terms of thermodynamic behaviour, kinetic control, and the structural quality needed to access quantum confinement effects. The answer, with appropriate qualifications, is yes. Thermodynamically, all five precursors are spontaneous carbon sources above 575–620 C temperatures that place CCVD firmly within reach of standard equipment. The differences in ΔH and ΔS between precursors are real but modest, and they translate into predictable differences in the lower boundary of the useful synthesis temperature rather than categorical changes in feasibility. Kinetically, the window between 750 and 920 C emerges as the productive regime across all catalyst-precursor combinations studied, with the specific position of the yield maximum shifting by 20–40 C depending on the precursor oxygen content and catalyst metal. Activation energies in the range 105–119 kJ mol^{-1} place these systems in the surface-diffusion-limited kinetic regime, which is the same regime that governs high-quality CVD growth from methane or ethylene.

The quantum confinement data are perhaps the most practically significant result. Green-synthesised SWCNTs with diameters below 3 nm follow the tight-binding bandgap scaling within experimental uncertainty, and those below 1.8 nm produce resolvable PLE emission features attributable to specific (n, m) chirality pairs. The diameter range accessed in these experiments, 0.9–4.1 nm, overlaps substantially with the range needed for near-infrared photovoltaic and single-photon emitter applications.

The principal limitation relative to conventional CVD remains defect density: I
The principal limitation relative to conventional CVD remains defect density: I_D/I_G ratios are consistently 0.15–0.25 higher than for methane-derived material at comparable synthesis temperatures. Preliminary annealing experiments show this gap is not fixed, and a systematic study of post-synthesis treatment conditions is warranted. On the catalyst side, bimetallic Fe-Co on Al_2O_3 consistently outperformed single-metal systems in both yield and diameter control, pointing toward further exploration of ternary catalyst compositions.

Two further directions appear worth pursuing. First, the relationship between precursor molecular architecture and the chirality distribution of the resulting SWCNTs deserves more detailed investigation. The current data suggest that oxygen-rich precursors may favour near-armchair growth through a nucleation mechanism that is not yet understood at the atomic scale. Second, scaling the process beyond the 50 mg catalyst bed used here will require addressing the heat and mass transfer challenges that emerge in larger reactors, particularly for solid precursors such as bagasse extract where aerosol delivery is less straightforward than for liquids or gases.

ACKNOWLEDGEMENTS

The authors thank the Central Nanofabrication Facility at IIT Delhi for access to HRTEM and Raman instruments, for constructive discussion regarding PLE data interpretation.

REFERENCES

[1] S. Iijima and T. Ichihashi, "Single-shell carbon nanotubes of 1-nm diameter," *Nature*, vol. 363, pp. 603–605, 1993.

[2] M. S. Dresselhaus, G. Dresselhaus, R. Saito, and A. Jorio, "Raman spectroscopy of carbon nanotubes," Phys. Rep., vol. 409, no. 2, pp. 47–99, 2005.

[3] R. Campana, L. Fernandez-Santos, and J. Villalba, "Thermodynamic feasibility of glucose-derived carbon nanotubes via low-temperature CVD," Carbon, vol. 194, pp. 112–123, 2022.

[4] T. Nakamura and K. Sato, "Ethanol-based catalytic synthesis of single-walled carbon nanotubes using supported nickel catalysts," Carbon, vol. 202, pp. 78–91, 2023.

[5] K. Osei-Wusu, P. O. Mensah, and E. Amoah, "Photoluminescence signatures of quantum confinement in bio-synthesised single-walled carbon nanotubes," Nanoscale, vol. 16, no. 4, pp. 1892–1903, 2024.

[6] R. Saito, G. Dresselhaus, and M. S. Dresselhaus, Physical Properties of Carbon Nanotubes. London, U.K.: Imperial College Press, 1998.

[7] R. E. Smalley and B. I. Yakobson, "The future of the fullerenes," Solid State Commun., vol. 107, no. 11, pp. 597–606, 1998.

[8] S. M. Bachilo et al., "Structure-assigned optical spectra of single-walled carbon nanotubes," Science, vol. 298, pp. 2361–2366, 2002.

[9] T. Ando, "Excitons in carbon nanotubes revisited: Dependence on diameter, Aharonov–Bohm flux, and strain," J. Phys. Soc. Jpn., vol. 75, no. 2, p. 024707, 2006.

[10] M. J. Bronikowski et al., "Gas-phase production of carbon single-walled nanotubes from carbon monoxide via the HiPco process," J. Vac. Sci. Technol. A, vol. 19, no. 4, pp. 1800–1805, 2001.

[11] Y. Li et al., "Growth of single-walled carbon nanotubes from discrete catalytic nanoparticles of various sizes," J. Phys. Chem. B, vol. 105, no. 46, pp. 11424–11431, 2001.

[12] P. T. Reilly and W. B. Whitten, "The role of free radical intermediates in the production of carbon nanotubes during the hydrocarbon CVD process," Carbon, vol. 44, no. 9, pp. 1653–1660, 2006.

[13] A. Moisala, A. G. Nasibulin, and E. I. Kauppinen, "The role of metal nanoparticles in the catalytic production of single-walled carbon nanotubes—A review," J. Phys.: Condens. Matter, vol. 15, no. 42, p. S3011, 2003.

[14] M. S. Dresselhaus, G. Dresselhaus, and P. Avouris, Eds., Carbon Nanotubes: Synthesis, Structure, Properties, and Applications. New York, NY, USA: Springer, 2001.

[15] R. L. Vander Wal, G. M. Berger, and T. M. Ticich, "Carbon nanotube synthesis in a flame using laser ablation for in situ catalyst generation," Appl. Phys. A, vol. 77, pp. 885–889, 2003.

[16] W. E. Alvarez et al., "Characterization of single-walled carbon nanotubes (SWNTs) produced by CO disproportionation on Co–Mo catalysts," Chem. Mater., vol. 14, no. 4, pp. 1853–1858, 2002.

[17] A. M. Cassell, J. A. Raymakers, J. Kong, and H. Dai, "Large-scale CVD synthesis of single-walled carbon nanotubes," J. Phys. Chem. B, vol. 103, no. 31, pp. 6484–6492, 1999.

[18] I. W. Chiang et al., "Purification and characterization of single-wall carbon nanotubes (SWNTs) obtained from the gas-phase decomposition of CO (HiPco process)," J. Phys. Chem. B, vol. 105, no. 35, pp. 8297–8301, 2001.

[19] M. Meyyappan, Carbon Nanotubes: Science and Applications. Boca Raton, FL, USA: CRC Press, 2005.

[20] M. M. A. Rafique and J. Iqbal, "Production of carbon nanotubes by different routes—A review," J. Encapsulation Adsorption Sci., vol. 1, no. 2, pp. 29–34, 2011.

[21] A. Thess et al., "Crystalline ropes of metallic carbon nanotubes," Science, vol. 273, pp. 483–487, 1996.

[22] G. Zhong et al., "Acetylene: A key growth precursor for single-walled carbon nanotube forests," J. Phys. Chem. C, vol. 113, no. 40, pp. 17321–17325, 2009.

[23] R. Xiang et al., "Carbon atoms in ethanol do not contribute equally to formation of single-walled carbon nanotubes," ACS Nano, vol. 7, no. 4, pp. 3095–3103, 2013.

[24] K. S. Ibrahim, “Carbon nanotubes—Properties and applications: A review,” Carbon Lett., vol. 14, no. 3, pp. 131–144, 2013.
[25] I. Maurin et al., “On the origin of the G-band broadening and D-band intensification observed in Raman spectra of multi-walled carbon nanotubes,” Carbon, vol. 214, p. 118363, 2023.
[26] C. Ramírez et al., “Synthesis of carbon nanotubes and graphene from biomass-derived precursors: An updated review,” Carbon, vol. 223, p. 119042, 2024.
[27] H. Wang et al., “Quantum transport properties of narrow carbon nanotubes synthesised from bio-derived ethanol at near-atmospheric pressure,” ACS Appl. Nano Mater., vol. 7, no. 3, pp. 3412–3424, 2024.